Water Resources Research

RESEARCH ARTICLE
10.1029/2023WR035217

Impacts of Channel-Spanning Log Jams on Hyporheic Flow

S. H. Huang[1,2] and J. Q. Yang[1,2]

[1]Saint Anthony Falls Laboratory, University of Minnesota, Minneapolis, MN, USA, [2]Department of Civil, Environmental, and Geo-Engineering, University of Minnesota, Minneapolis, MN, USA

Key Points:

- The hyporheic flow velocity in a channel with a log jam was two orders of magnitude higher than that of a bare channel
- At Froude numbers (*Fr*) above 0.06, the nondimensional log jam-induced hyporheic flux increased by a factor of five with increasing *Fr*
- Similar to the hyporheic flux, the water surface profile and turbulence intensity changed noticeably at *Fr* above 0.06

Supporting Information:

Supporting Information may be found in the online version of this article.

Correspondence to:

J. Q. Yang,
judyyang@umn.edu

Citation:

Huang, S. H., & Yang, J. Q. (2023). Impacts of channel-spanning log jams on hyporheic flow. *Water Resources Research*, *59*, e2023WR035217. https://doi.org/10.1029/2023WR035217

Received 2 MAY 2023
Accepted 17 OCT 2023

Abstract In-stream wood structures, such as single logs, river steps, and debris dams, are known to drive hyporheic flow, defined as the flow that goes into the subsurface region and then back to the free-flowing surface water. The hyporheic flow plays an important role in regulating water quality and biogeochemical cycles in rivers. Here, we investigated the impact of a channel-spanning porous log jam, representing piles of wood logs, on hyporheic flow through a combination of direct visualization and theories. Specifically, we developed a method using refractive index-matched sediment to directly visualize the hyporheic flow around and below a porous log jam, formed by piles of cylindrical rods, in a laboratory flume. We tracked the velocity of a fluorescent dye moving through the transparent sediment underneath the log jam. In addition, we measured the water surface profile and the spatially varying flow velocity near the log jam. Our results show that the normalized log jam-induced hyporheic flux remained smaller than 10% at Froude numbers (*Fr*) below 0.06 and increased by a factor of five with increasing *Fr* at $Fr > 0.06$. We combined the mass and momentum conservation equations of surface flow with Darcy's equation to explain the dependency of the log jam-induced hyporheic flux on *Fr*. Further, we observed that at $Fr > 0.06$, the water surface dropped noticeably and the turbulent kinetic energy increased immediately on the downstream side of the log jam. These findings will facilitate future quantification of hyporheic flow caused by channel-spanning porous log jams.

Plain Language Summary Log jams are trees that frequently fall and accumulate in rivers. Field surveys and numerical simulations suggest that log jams slow down the surface flow and drive hyporheic flows, which are bidirectional flows that go into the riverbed and back to the surface water. Hyporheic flows carry pollutants and nutrients and thus play a critical role in water quality and river biogeochemical cycles. Despite the importance of hyporheic flows, the quantitative characterization of log jam-induced hyporheic flows remains incomplete. In this study, we conducted experiments in a water-recirculating flume with a log jam model that resembles piles of wood logs commonly found in rivers. We injected a fluorescent dye into a transparent sediment bed made from hydrogel beads and visualized the flow within the sediment bed. Our experimental results show that log jams can increase the hyporheic flow rate by one order of magnitude. Further, we developed a theoretical model to explain the hyporheic flow induced by a log jam. Our experimental results and theoretical model will facilitate the evaluation of the impact of log jams on the fate and transport of nutrients and contaminants in rivers for future restoration projects.

1. Introduction

Hyporheic flow refers to the flow of surface water into the subsurface or sediment region and back to the free-flowing surface water (Boano et al., 2014; Gooseff, 2010; Tonina, 2012). Enhanced hyporheic flow increases the retention time of solutes (Marion et al., 2002; Stonedahl et al., 2012), organic matter (Boulton et al., 1998; Schaper et al., 2019), and fine particles (Drummond et al., 2020; Packman et al., 2000) in the streambeds. Consequently, hyporheic flow alters nutrient uptake by benthic stream organisms (Lehane et al., 2002) and plays an important role in the biogeochemical cycle (Boano et al., 2010; Li et al., 2017). In addition, hyporheic flow alters the adsorption and degradation of contaminants by sediment and microbes and thus controls the fate of contaminants in streams (Jaeger et al., 2021; McCallum et al., 2020).

Hyporheic flows can be induced by many factors, such as bed forms (Buffington & Tonina, 2009; Dudunake et al., 2020; Elliott & Brooks, 1997; Marion et al., 2002; Packman et al., 2004; Tonina & Buffington, 2007), channel sinuosity (Boano et al., 2006; Cardenas, 2009), turbulence (Roche et al., 2018, 2019; Rousseau & Ancey, 2020; Voermans et al., 2017, 2018b), and in-channel components like vegetation (Huang & Yang, 2022; Jin et al., 2023; Yuan et al., 2021) and in-stream wood (Ader et al., 2021; Doughty et al., 2020; Lautz et al., 2006; Sawyer et al., 2011; Wilhelmsen et al., 2021).

In-stream wood, including single tree trunks or logs and an accumulation of logs, is ubiquitous in forested river corridors (Ismail et al., 2021) and play an important role in the transport of water, solutes, organic matter, and sediment (Spreitzer et al., 2021; Wohl, 2016). In-stream wood can increase the flow resistance (Ader et al., 2021; Wohl & Scamardo, 2021), which slows down the surface flow velocity (Lautz et al., 2006) and causes a difference in the water surface elevation along the stream bed (Follett et al., 2021; Schalko et al., 2018). The pressure gradient due to this difference in water surface elevation can drive hyporheic flows (Ader et al., 2021; Doughty et al., 2020; Lautz et al., 2006; Wilhelmsen et al., 2021).

The impacts of a variety of structures formed by in-stream wood, including single channel-spanning logs (Sawyer et al., 2011; Wallerstein & Thorne, 2004), river steps (Curran & Wohl, 2003; Endreny et al., 2011; Scott et al., 2014), and debris dams (Janzen & Westbrook, 2011; Lautz et al., 2006; Majerova et al., 2015), on hyporheic flow have been studied. Sawyer et al. (2011) quantified the hyporheic flow induced by a single channel-spanning log through numerical simulations and flume experiments. Endreny et al. (2011) quantified the hyporheic flow paths created by a river step through laboratory experiments and hydrodynamic simulation. The impacts of the debris dams on the hyporheic flows have been studied by field surveys and numerical modeling (Janzen & Westbrook, 2011; Lautz et al., 2006; Majerova et al., 2015). In addition to the above-mentioned structures, wood logs can pile up and form a porous structure that blocks the whole water column; such structures, hereafter referred to as porous log jams, are also known to induce hyporheic flow (Doughty et al., 2020; Wilhelmsen et al., 2021). However, systematic quantification of the hyporheic flow induced by a porous log jam remains lacking. The goal of this study is to investigate the impact of a channel-spanning porous jam, formed by piles of logs, on hyporheic flow through a combination of laboratory experiments and theoretical analyses.

To quantify the hyporheic flow induced by a channel-spanning porous log jam, we directly visualize and quantify the bi-directional hyporheic flows induced by the jam through laboratory experiments using refractive index-matched materials. Specifically, we created an optically accessible channel using transparent hydrogel beads to simulate sediment and translucent acrylic rods to simulate a porous log jam. We injected fluorescent dye, illuminated the dye with a light-emitting diode (LED) lamp, and traced the movement of the dye using a digital camera. From the velocities of the dye migration, we quantified the log jam-induced hyporheic flow velocities. In addition, we measured the surface flow velocity in detail around the log jam using particle image velocimetry (PIV). Furthermore, we developed a physically based theoretical model to explain the dependency of log jam-induced hyporheic flow on Froude number.

2. Theories

2.1. The Log Jam-Induced Changes in the Surface Flow

As the surface water flows into a porous log jam, the surface flow slows down due to the drag exerted by the log jam. As a result of this momentum loss, the water surface elevation on the upstream side of the log jam becomes higher than that on the downstream side of the log jam. The water surface profile around a log jam over a solid impermeable bed has been characterized by Follett et al. (2020) based on the momentum balance of the surface flow in the streamwise direction. Specifically, consider the void or pore space of the log jam as a control volume and assume that the mean vertical surface flow velocity in the log jam is negligible; the rates of momentum of the surface flow across the upstream and downstream boundaries of the log jam are $\rho B(1-\phi_j)H_{\text{up}}U_{\text{up}}^2$ and $\rho B(1-\phi_j)H_{\text{down}}U_{\text{down}}^2$ (kg $\cdot$ m/s^2), respectively. Here ρ is the water density (kg/m^3); B is the channel width (m); ϕ_j is the solid fraction of the log jam; H_{up} and H_{down} are the water depths (m) on the upstream and downstream sides of the log jam, respectively; and U_{up} and U_{down} are the mean surface flow velocities in the streamwise direction on the upstream and downstream sides of the log jam (m/s), respectively.

At steady state, two major external forces contribute to the net momentum change of the surface flow through the log jam in the streamwise direction: the force due to hydrostatic pressure and the drag force exerted by the solid boundaries of the log jam. The net hydrostatic force acting on the surface flow in the log jam is $\frac{1}{2}\rho g B(1-\phi_j)\left(H_{\text{up}}^2 - H_{\text{down}}^2\right)$ (kg $\cdot$ m/s^2). Here g is the gravitational acceleration (m/s^2).

First, we assume that the drag of the porous jam, consisting of piles of dowels, can be approximated from the empirical equations developed for an array of vertical cylindrical dowels (see Section 5.4 for details). Specifically, we approximate the drag force exerted by the log jam on the surface flow using a quadratic drag law, that is, $\frac{1}{2}\rho B L_j C_D a H_{\text{down}} U_{\text{log}}^2$ (kg $\cdot$ m/s^2) (Follett et al., 2020). Here L_j is the length of the log jam in the streamwise direction

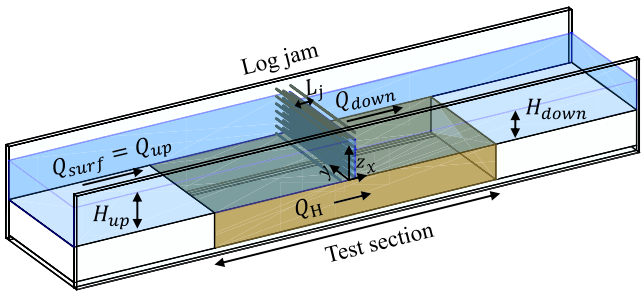

Figure 1. Schematic diagram of the experimental setup and the two-chamber model. Specifically, we divide the flows into the surface chamber (blue) and the subsurface chamber filled with sediment (brown). The x, y, and z axes represent the streamwise, spanwise, and vertical directions, respectively. $z = 0$ indicates the sediment-water interface. $x = 0$ indicates the center of the log jam in the streamwise direction. L_j represents the length of the log jam in the streamwise direction.

(m); C_D is the drag coefficient of the log jam. C_D depends on the Reynolds number of the surface flow within the log jam. We estimate C_D using Equation 14 in Cheng and Nguyen (2011) ($C_D = 50/Re_v^{0.43} + 0.7\left[1 - e^{-Re_v/15{,}000}\right]$). Re_v is the Reynolds number based on the frontal area of the log jam, that is, $Re_v = U_{\log} r_v/\nu$ (Cheng & Nguyen, 2011), in which r_v is the modified hydraulic radius defined as $r_v = \frac{\text{log jam volume}}{\text{effective wetted area of logs}} = a^{-1}$; a is the frontal area per jam volume (m^{-1}); υ is the kinematic viscosity of the fluid (m^2/s), and $U_{\log}$ is the spatially averaged surface flow velocity in the streamwise direction in the porous log jam (m/s). To simplify the equation, we approximate $U_{\log}$ as $U_{\text{down}}/(1-\phi_j)$. In Section 5.4, we verified this assumption using our experimental measurements, showing that the difference between $U_{\log}$ and the surface flow velocity at the downstream edge of the log jam, $U_{\text{down}}/(1-\phi_j)$, was less than 5% of $U_{\log}$. Furthermore, we assume that the drag exerted by the side walls and the bed are small compared to the log jam-induced drag (Follett et al., 2020). As a result, the momentum balance equation in the streamwise direction for the flow in the surface water can be written as,

$$\frac{1}{2}\rho g B(1-\phi_j)\left(H_{\text{up}}^2 - H_{\text{down}}^2\right) - \frac{1}{2}\rho B L_j C_D a H_{\text{down}} U_{\log}^2 = \rho B(1-\phi_j)\left(H_{\text{down}} U_{\text{down}}^2 - H_{\text{up}} U_{\text{up}}^2\right). \quad (1)$$

Previous studies show that the momentum change, $\rho B(1-\phi_j)\left(H_{\text{down}} U_{\text{down}}^2 - H_{\text{up}} U_{\text{up}}^2\right)$, was about one order of magnitude smaller than the left-hand terms of Equation 1 and can be ignored (Follett et al., 2020, 2021). Consistently, our experiments show that this momentum term was only 1% of the hydrostatic pressure force $\frac{1}{2}\rho g B(1-\phi_j)\left(H_{\text{up}}^2 - H_{\text{down}}^2\right)$ (see Section 5.4 for details). Thus, we eliminate this term and simplify Equation 1 as:

$$\frac{1}{2}\rho g B(1-\phi_j)\left(H_{\text{up}}^2 - H_{\text{down}}^2\right) - \frac{1}{2}\rho B L_j C_D a H_{\text{down}} U_{\text{down}}^2/(1-\phi_j)^2 = 0 \quad (2)$$

2.2. The Log Jam-Induced Hyporheic Flow

Here we propose a two-chamber model, one for the surface flow and the other one for the subsurface flow (see Figure 1), to characterize the hyporheic flow rate induced by a log jam. In the surface chamber, the surface flow rate approaching the log jam is $Q_{\text{surf}} = U_{\text{up}} B H_{\text{up}}$. In the subsurface chamber, we use Darcy's equation to estimate the hyporheic flow rate, namely $Q_H = -\frac{k}{\mu}\frac{\partial P}{\partial x} B H_s$, with k denoting the permeability of the sediment bed (m^2); μ denoting the dynamic viscosity of the fluid (Pa · s), and $\frac{\partial P}{\partial x}$ denoting the pressure gradient (Pa/m) along the streamwise (x) direction. H_s is the sediment depth (m). To simplify the Darcy's equation, we assume that the hydraulic pressure difference caused by the difference between the surface flow velocities on the upstream and downstream sides of the log jam, $\frac{1}{2}\rho\left(U_{\text{down}}^2 - U_{\text{up}}^2\right)$, is orders of magnitude smaller than the difference in the hydrostatic pressure difference at the sediment-water interface, $\rho g\left(H_{\text{down}} - H_{\text{up}}\right)$. Justification for this hypothesis is presented in Section 5.4. As a result, $\frac{\partial P}{\partial x}$ can be estimated from the gradient in the hydrostatic pressure at the sediment-water interface, namely, $\frac{\partial P}{\partial x} = \frac{\Delta p}{L_s} = -\frac{\rho g \Delta H}{L_s}$ with $\Delta H = H_{\text{up}} - H_{\text{down}}$ denoting the difference in water depth on the upstream and downstream sides of the log jam and L_s denoting the mean length scale of the hyporheic flow induced by the log jam. Accordingly, the hyporheic flow rate can be approximated as:

$$Q_H = \frac{k}{\mu}\frac{\rho g \Delta H}{L_s} B H_s. \quad (3)$$

In this study, L_s is a parameter determined by Darcy's law; such a definition is different from the definition based on the physical length of the region influenced by the hyporheic flow used in previous studies (e.g., Elliott & Brooks, 1997). We expect our L_s to be determined by many parameters, including the log jam length and the spatial constraint of the sediment boundaries. In this study, we assume that L_s is approximately the same because the log jam and sediment were the same for all the cases. Note that the flume boundaries on the upstream and downstream sides of the sediment bed in the test section were impermeable in this study (Figure 1). By dividing

Equation 2 by $\frac{1}{2}\rho g B(1-\phi_j)$, we obtain the following Equation 4a. In addition, the relationship between surface flow and subsurface flow can be described by conservation of mass, that is, $Q_{\text{surf}} = Q_{\text{up}} = U_{\text{up}} B H_{\text{up}} = Q_H + Q_{\text{down}}$ (Equation 4b).

$$\begin{cases} H_{\text{up}}^2 - H_{\text{down}}^2 - \frac{L_j C_D a}{g(1-\phi_j)^3} H_{\text{down}} U_{\text{down}}^2 = 0 & \text{(4a)} \\ H_{\text{up}} U_{\text{up}} - H_{\text{down}} U_{\text{down}} + \frac{k}{\mu} \frac{\rho g (H_{\text{down}} - H_{\text{up}})}{L_s} H_s = 0. & \text{(4b)} \end{cases}$$

By dividing both sides of Equation 4a by $H_{\text{up}} + H_{\text{down}}$, we derive following Equation 5, which suggests that the difference in water surface elevations on the upstream and downstream sides of the log jam increases with the Froude number on the downstream side of the porous log jam, namely,

$$H_{\text{up}} - H_{\text{down}} = \Delta H = \frac{H_{\text{down}}^2}{(H_{\text{up}} + H_{\text{down}})} \frac{L_j C_D a}{(1-\phi_j)^3} Fr^2 \tag{5}$$

with $Fr^2 = U_{\text{down}}^2 / g H_{\text{down}}$. Further dividing both sides of Equation 5 by H_{down}, and substituting H_{up} with $H_{\text{down}} + \Delta H$, we obtain a quadratic equation with unknown $\frac{\Delta H}{H_{\text{down}}}$, that is, $\left(\frac{\Delta H}{H_{\text{down}}}\right)^2 + 2\left(\frac{\Delta H}{H_{\text{down}}}\right) - \frac{L_j C_D a}{(1-\phi_j)^3} Fr^2 = 0$ (detailed derivation is shown in Text S1 of the Supporting Information S1). This equation has two analytical solutions, and the solution with positive H_{up} ($\Delta H + H_{\text{down}} > 0$) is:

$$\frac{\Delta H}{H_{\text{down}}} = -1 + \sqrt{1 + \frac{L_j C_D a}{(1-\phi_j)^3} Fr^2}. \tag{6}$$

Equation 6 suggests that the difference in the water surface elevation nondimensionalized by the downstream water surface elevation, $\Delta H / H_{\text{down}}$, increases with increasing Froude numbers.

Finally, by substituting Equation 5 into Equation 3, we can write the hyporheic flow rate induced by a log jam as:

$$Q_H = \frac{H_{\text{down}}^2}{(H_{\text{up}} + H_{\text{down}})} \frac{\rho g k H_s B}{L_s \mu} \frac{L_j C_D a}{(1-\phi_j)^3} Fr^2. \tag{7}$$

Equation 7 suggests that the log jam-induced hyporheic flow rate also increases with the square of the Froude number. The dependency of hyporheic flow flux on Fr^2 has previously been proposed for single logs (Sawyer et al., 2011). We compared our model and their model in Text S2 of the Supporting Information S1. Good agreement was observed between these two models, suggesting that our model can potentially be used to evaluate the impacts of other wood structures, such as single logs, on the hyporheic flow.

3. Materials and Methods

We conducted experiments in a 14.0 m long, 0.6 m wide, and 0.3 m deep water-recirculating flume in the Saint Antony Falls Laboratory at the University of Minnesota. The channel had a horizontal bottom and glass walls. The flow was driven by four thrusters (T200 Thruster; BlueRobotics, California). To measure the impacts of log jam on hyporheic flow, we placed a log jam block (described below) above a 1.5 m-long, 0.6 m-wide, and 18 cm-deep sediment bed in a straight test section of the flume (Figures 1 and 3a). The sediment was made of refractive index-matched hydrogel beads of 5.6 ± 0.6 mm diameter. The porosity of the sediment bed was $\phi_s = 0.3$. We estimated the permeability k of the hydrogel beads using the Karman-Cozeny relationship that $k = \phi_s^3 d_s^2 / 180(1-\phi_s)^2 = 9.6 \times 10^{-3}$ mm^2, with d_s being the diameter of the hydrogel beads (Voermans et al., 2018a). The flume boundaries on the upstream and downstream sides of the sediment bed were impermeable acrylic boards. The permeability of our sediment resembled the typical range of a gravel bed, which is $k = 3 \times 10^{-5}$ to 10^{-1} mm^2 (Das, 2021; Naganna et al., 2017). A plastic polyester mesh with a pore size of 4 mm was placed at the top of the sediment bed to keep the hydrogel beads in place.

The channel-spanning porous log jam was made by piling acrylic cylinders in an acrylic frame and gluing the dowels using a super glue (AD119; Scotch Brand, Minnesota), as shown in Figure 2a. The frame was used to

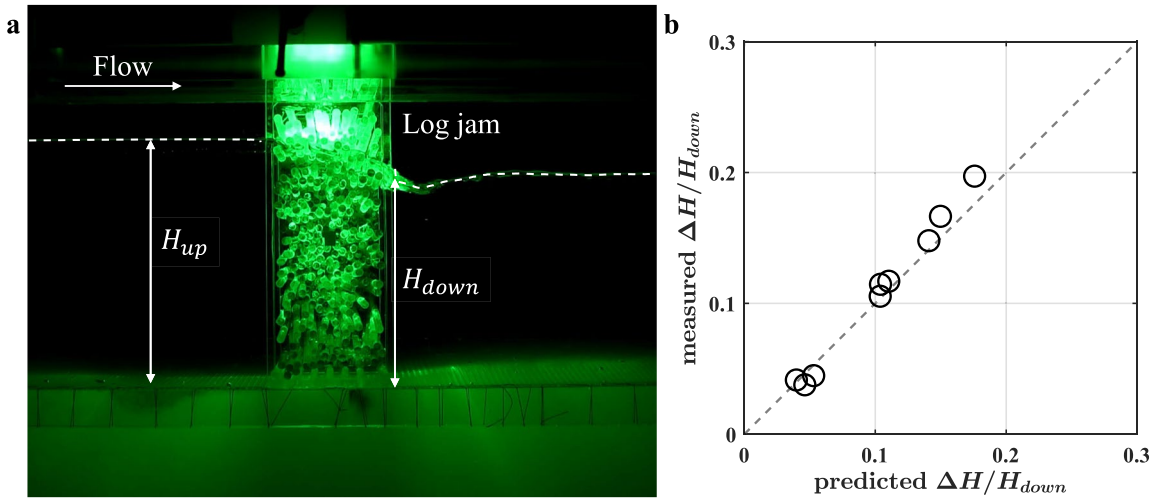

Figure 2. The change in water surface elevation due to a channel-spanning porous log jam. (a) The water surface (the white dashed lines) was illuminated by a laser sheet. (b) The predicted difference in the water surface elevation normalized by the downstream water depth versus the measured non-dimensional value. ΔH indicates the difference between the water surface elevation on the upstream and downstream sides of the log jam, that is, $\Delta H = H_{\text{up}} - H_{\text{down}}$. The dimensionless value $\Delta H/H_{\text{down}}$ in the x-axis was predicted using Equation 6.

keep the dowels in place and consisted of six 4-mm-wide bars placed equally spaced along the cross-sectional area of the flume on the upstream and downstream sides of the jam. Experiments with the frame but no log jams show that the frame had a negligible effect on the water surface profile (Figure S3 in Supporting Information S1). The diameter and length of the acrylic dowels were 6.4 ± 0.1 mm and 38.0 ± 0.1 cm, respectively. The length of the log jam L_j was 9.0 cm (Figure 1). The solid volume fraction of the jam ϕ_j was defined as the ratio between the solid volume of the dowels and the total jam volume, including pore space and the dowels (Follett et al., 2021). The solid volume fraction of our jam was 0.42, consistent with the typical range of the log jam found in the field $\phi_j = 0.2$ to 0.7 (Dixon, 2016; Livers et al., 2020; Schalko et al., 2018; Spreitzer et al., 2020). The frontal area per jam volume $a = 4\phi_j/\pi d = 84.4$ m^{-1} for cylinders (Nepf, 2012). Here $d = 6.4$ mm was the diameter of the acrylic dowels. The water surface was lower than the top of the log jam during the experiments.

To evaluate the impact of a log jam on hyporheic flow, we ran water through the channel using four thrusters mounted equally spaced along a cross-sectional area of the channel (T200 Thruster; BlueRobotics, California). The initial water depth was set to 12, 16, or 20 cm before the flow started. For each initial water depth, we conducted experiments at three surface flow rates (Table 1). During the experiments with flows, the water surface on the downstream side of the log jam dropped due to log jam-induced drag (Figure 2a). To capture this surface drop, we illuminated the water surface with a laser and imaged the water surface using a side-looking Nikon camera (D7500; Nikon, Japan) from 15 cm upstream to 15 cm downstream of the log jam. We identified the water surface based on the pixel intensity because the water surface has a much larger pixel intensity due to the reflection of the laser light at the water surface (Figure 2a). We traced the water surface profile based on the intensity of the pixels (see Text S3 and Figure S4 in Supporting Information S1 for details). The code used to process the data has been uploaded to the Data Repository for the University of Minnesota (DRUM). A small vibration of the water surface, or surface wave, was observed during the experiments. To remove this surface vibration, we recoded the images at a 60 Hz frame rate for 30 s and calculated the temporally averaged water surface by averaging the surface elevation identified from 1,800 images. The standard deviation of water surface variation is shown in Figure S5a of the Supporting Information S1. Our analysis shows that 30 s are enough to obtain a convergent profile of the water surface elevation (Figure S5b in Supporting Information S1).

We also measured the streamwise and vertical surface flow velocities using two-dimensional (2D) particle image velocimetry (PIV) across the flume 1 m upstream and 2 cm downstream of the log jam (Figure 3). The cross Section 1 m upstream of the log jam was on an impermeable bed. The cross Section 2 cm downstream of the log jam was the cross section closest to the log jam that we could measure using the PIV. The custom-built PIV consists of a 2-mm-thick green laser sheet of 2-W energy at 532 nm (LSR532F; Lasever, China) and a side-looking camera with a maximum resolution of 1,224 × 1,024 pixels (BFS-U3-51S5M-C; FLIR Systems, Wilsonville). The field of view of the camera was 4 cm × 20 cm in the middle of the channel ($y = 30$ cm). To

Table 1
The Experimental Parameters

	Case No.	H_{up} (cm)	H_{down} (cm)	U_{up} (cm/s)	U_{down} (cm/s)	U_H (cm/s)	$Q_{H,PIV}$ (cm^3/s)	$Q_{H,Dye}$ (cm^3/s)	Fr[a]	Re_v[b]
Cases with a log jam	L1	19.8	17.0	8.1	7.9	1.09	2,029	1,202	0.061	1,621
	L2	20.1	18.0	5.9	6.4	0.53	204	582	0.049	1,323
	L3	20.0	19.2	3.6	3.6	0.27	205	296	0.026	739
	L4	16.4	13.7	7.9	7.7	1.05	2,472	1,160	0.066	1,577
	L5	15.9	13.9	6.0	6.7	0.62	467	679	0.057	1,372
	L6	16.0	15.4	3.6	3.5	–	276	–	0.028	708
	L7	12.1	11.0	4.4	4.7	–	177	–	0.046	968
	L8	12.1	10.8	4.6	4.9	–	231	–	0.047	999
	L9	12.1	11.5	3.1	3.1	–	97	–	0.030	645
Cases with a flat bed	F1	19.4	19.5	8.2	8.6	–	−241	0.8	0.062	–
	F2	19.7	19.7	9.7	9.9	–	−108	–	0.071	–
	F3	15.5	15.5	11.8	11.9	–	−108	–	0.096	–
	F4	11.7	11.7	7.0	7.0	–	0	–	0.066	–
Case with a bedform	B1	19.8[c]	19.5[c]	8.3	8.5	–	−69	1.9	0.061	–

[a]$Fr = U_{down}/\sqrt{gH_{down}}$. [b]$Re_v = U_{log} r_v/\nu$, where $r_v = \frac{\text{water volume}}{\text{effective wetted area}} = a^{-1} = 0.012$ m. ν is kinematic viscosity of water. [c]The water depths for Case B1 were measured by a ruler.

measure the surface flow velocity, the water was seeded with solid glass beads with a specific gravity of 2.6 and a mean diameter of 35 μm (3000 E-Spheriglass; Potters Industries Inc., Pennsylvania). An 8-cm-wide square plastic box was placed on the water surface to prevent image distortion due to the moving water surface. Images were taken at 200 Hz for 50 s by the side-looking camera. To calculate the surface flow velocity, we processed the images using the software PIVLab developed by Thielicke and Sonntag (2021). For the two cross sections, surface flow velocity profiles were measured at a 5 cm interval in the spanwise direction (y-axis in Figure 1) with additional locations close to the wall (Figure S6 in Supporting Information S1). To calculate the surface flow rate, we interpolated the measured mean surface flow velocities to the points on a 1-cm grid and integrated the

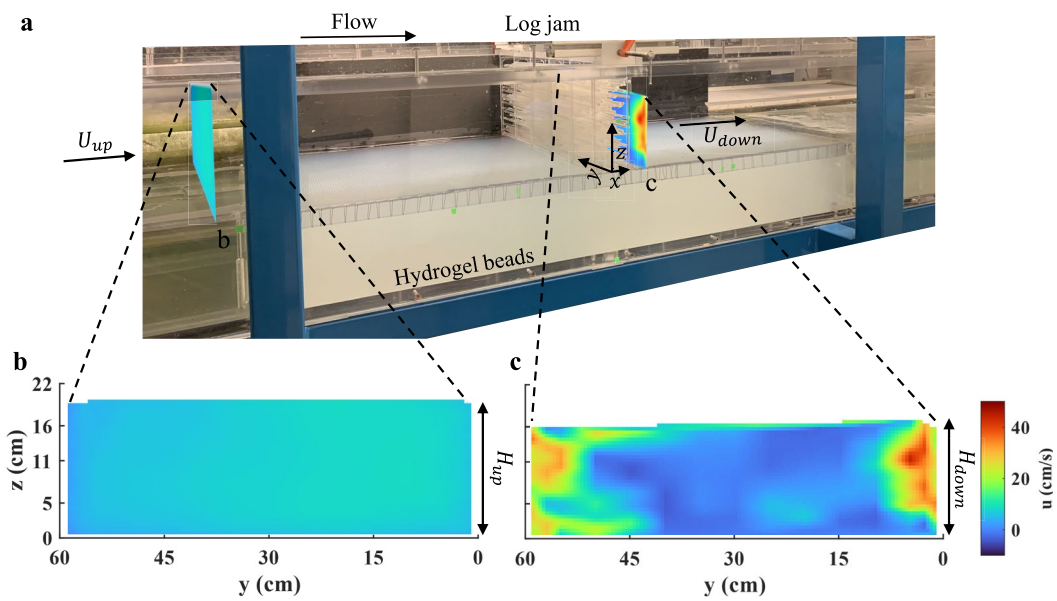

Figure 3. (a) The flow velocities 1 m upstream and 2 cm downstream of the log jam were measured using a PIV. (b) The flow field on the upstream side of the log jam. (c) The flow field on the downstream side of the log jam. The locations of the flow measurements in the spanwise direction are described in Section 3 and Figure S6 in Supporting Information S1.

interpolated surface flow velocity over the whole cross-sectional area (Text S4 and Figure S8 in Supporting Information S1). The hyporheic flow rate measured using PIV was calculated as the difference between the surface flow rates on the upstream and downstream sides of the log jam, that is, $Q_{H,PIV} = Q_{\text{up}} - Q_{\text{down}}$. In addition, to evaluate the impact of the transition from impermeable to permeable bed on the surface flow, we measured the surface flow velocity along a streamwise transect in the middle of the channel without a log jam.

To directly measure the hyporheic flow within the sediment, we conducted dye visualization experiments to map the hyporheic flow path induced by the log jam and estimated the hyporheic flow velocity. We injected 1 mL of fluorescent dye at 1.0×10^{-3} wt% (Fluorescein, Sigma-Aldrich F6377) at around 30 locations, 2.5 cm apart in the streamwise and vertical directions, at $y = 25$ cm in the sediment beneath the log jam. We chose $y = 25$ cm because it was close to the middle of the flume ($y = 30$ cm) and was the maximum distance from the wall where fluorescent signals from the dye were distinct from the background in the recorded images. When the dye was injected further away from the wall, the fluorescent signal became weaker due to a slight difference in the refractive index of the hydrogel beads and water. The fluorescent dye in the sediment was illuminated by a blue LED lamp (30 cm × 30 cm) placed beside the flume. The green light emitted by fluorescein was recorded by a side-looking camera at 60 fps (D7500; Nikon, Japan) with a green light filter (FGV9S; Thorlabs, Newton). The hyporheic flow velocity was calculated from trajectories of the dye; specifically, we calculate the velocity as the distance between the locations of the centroid of the dye plume boundary in subsequent images divided by the time step (Figure S10 in Supporting Information S1). Afterward, we interpolated the hyporheic flow velocity measured at discrete locations linearly onto a 0.1 cm by 0.1 cm grid. From the interpolated hyporheic flow velocity field, we calculated the streamwise depth-averaged hyporheic flow velocity, U_H, as the average flow velocity within the sediment bed at the downstream edge of the log jam. The hyporheic flow rate estimated in dye visualization experiments was $Q_{H,Dye} = BH_sU_H$. In addition to tracking dye velocities at $y = 25$ cm, we also injected dye at $y = 10$ cm to provide a clearer visual demonstration of the dye path in Figure 5. The comparison between hyporheic flow fields at $y = 10$ cm and $y = 25$ cm for Case L1 (Table 1) can be found in Figure S11 of the Supporting Information S1.

To investigate the turbulent intensity of the surface flow, we calculated the turbulent kinetic energy as the sum of the squares of vertical and longitudinal surface flow velocity fluctuations, that is, $k_t = \frac{1}{2}\left(\overline{u'^2} + \overline{w'^2}\right)$ with u' and w' denoting the velocity fluctuations of the surface flow in the streamwise and vertical directions, respectively. In this study, u' and w' were measured by a two-dimensional (2D) PIV. To justify that the estimated k_t reflects the total turbulent kinetic energy in three-dimensional (3D) space, we measured the three-dimensional flow velocities at 122 locations on the downstream side of a log jam using an Acoustic Doppler Velocimeter (ADV; Nortek Vectrino, Norway). These ADV measurements show that the lateral component of the velocity fluctuation of the surface flow, or v', only contributed 10% of the total turbulent kinetic energy k_t, specifically, $\left(\overline{u'^2} + \overline{w'^2}\right)/\left(\overline{u'^2} + \overline{w'^2} + \overline{v'^2}\right) = 0.91 \pm 0.03$ (standard deviation) (Figure S12 in Supporting Information S1). The above comparison suggests that the 2D PIV velocity measurements of the surface flow provide accurate estimation of the total turbulent kinetic energy of the surface flow on the downstream side of the log jam.

During the experiments with water flowing in the flume for the cases with the highest surface flow rate, we observed a scour hole on the upstream side of the log jam and deposition on the downstream side. The bedforms reached an equilibrium shape after 8 hr of flow (see Text S5 in Supporting Information S1 for details). To evaluate the hyporheic flow induced by the bedform and a flat bed (without a log jam for both cases), we measured the hyporheic flow rate by both PIV and dye visualization experiments in a channel with a flat bed and a channel with a log jam-induced bedform but without the log jam. For both cases, we set the mean surface flow velocity on the upstream side of the log jam $U_{up} = 8.2 \pm 0.1$ cm/s, the same as in Case L1 (Table 1).

Finally, we calculated the effective permeability of the jam k_j using Darcy's equation,

$$k_j = -\frac{q_j \mu L_j}{\Delta P_j} \tag{8}$$

Here q_j was the flux of the surface flow through the log jam per unit area (m/s), which was $q_j = Q_{\text{down}}/BH_{\text{down}}$. ΔP_j was the hydraulic head difference between the upstream and downstream edges of the log jam, estimated as $\Delta P_j = \frac{1}{2}\rho g\left(H_{\text{down}} - H_{\text{up}}\right) + \frac{1}{2}\rho\left(U_{\text{down}}^2 - U_{\text{up}}^2\right)$. The results calculated by assuming velocity heads were negligible was discussed in Section 5.3. In addition, we also calculated k_j using the Dupuit-Forchheimer equation $\frac{Q_{\text{down}}}{B} = -\frac{k_j \rho g}{\mu}\frac{H_{\text{down}}^2 - H_{\text{up}}^2}{2L_j}$.

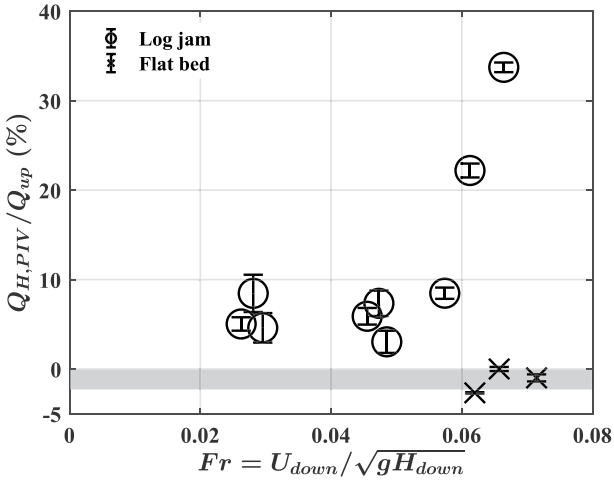

Figure 4. The hyporheic flow rate estimated from the PIV measurements versus the Froude number. The error bar indicates the uncertainty in integrating flow rate with different grid sizes (see Text S4 in Supporting Information S1 for details). The gray shaded area indicates the standard deviation of the hyporheic flow rate for the four cases with a flat bed.

4. Results

4.1. The Log Jam-Induced Change in the Water Surface Elevation

First, we measured the water surface elevation on the upstream and downstream sides of the channel-spanning log jam using a digital camera for cases with different surface flow velocities and water depths. A representative image for Case L1 (Table 1) is shown in Figure 2a. As shown in the image, the water surface on the upstream side of the log jam was 2.8 cm higher than the water surface on the downstream side of the jam. This difference in the water surface elevations on the upstream and downstream sides of the log jam was denoted as ΔH. For the three flow rates and three initial water depths considered here, the Froude number was in the range between 0.026 and 0.066 (Table 1). As shown in Figure S14a of the Supporting Information S1, the measured $\Delta H/H_{\text{down}}$ showed an increasing trend with the increases of the Froude number $Fr = U_{\text{down}}/\sqrt{gH_{\text{down}}}$. Based on Equation 6, we estimated the ratio of ΔH and the water surface elevation on the downstream side of the log jam, $\Delta H/H_{\text{down}}$, with the Froude number Fr, the log jam length L_j, the drag coefficient of the logs C_D estimated using Equation 14 in Cheng and Nguyen (2011), the frontal area pre jam volume a, and the solid fraction of the log jam ϕ_j. As shown in Figure 2b, the value predicted by Equation 6 and the measured $\Delta H/H_{\text{down}}$ agreed with each other, despite up to a 10% difference when $\Delta H/H_{\text{down}} > 0.15$ ($Fr > 0.06$). We anticipate that the underprediction of our model was because the turbulent kinetic energy of the surface flow increased sharply at $Fr > 0.06$ (see Section 5.1 for details), which dissipated more energy and likely increased the log jam drag. Despite the difference, Equation 6 predicted the $\Delta H/H_{\text{down}}$ with less than 10% uncertainty, confirming that the log jam-induced difference in water surface elevation ΔH was due to the log jam-induced drag and the associated loss in fluid momentum.

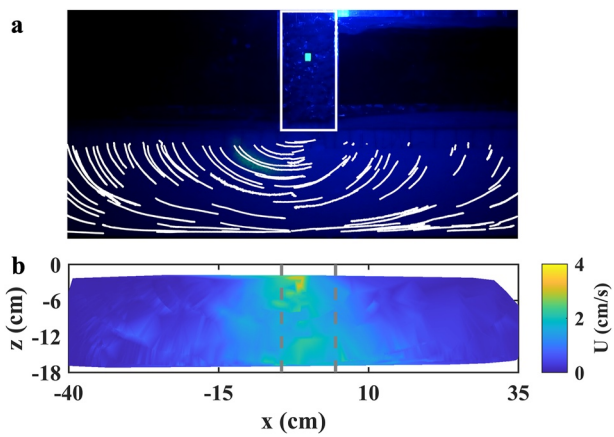

Figure 5. The hyporheic flow field under a log jam. (a) The trajectories (white lines in the bottom half of the image) of the dye obtained from time-lapse images (Figure S10 in Supporting Information S1). The white solid box indicates the boundary of the log jam. The green square in the middle of the white square box was a tape used to calibrate locations. (b) The hyporheic flow velocity field estimated from the trajectories. The color map indicates the hyporheic flow velocity in the streamwise direction. The origin of the z-axis was at the sediment-water interface. The origin of the x-axis was at the center of the log jam. The origin of the y-axis was at the right flume wall (when facing downstream). Gray dashed lines show the streamwise boundaries of the log jam. The case reported here was Case L1 (Table 1). The dye was injected at $y = 10$ cm for visualization purposes.

4.2. Hyporheic Flow Determined From the Surface Flow Fields

The upstream and downstream surface flow rates, that is, Q_{up} and Q_{down}, were calculated by integrating the streamwise surface flow velocity measured by a particle image velocimetry (PIV) over the cross-sectional area of the flume, as shown in Figure 3. Representative velocity fields on the upstream and downstream sides of the log jam measured by a PIV for Case L1 (Table 1) are shown in Figures 3b and 3c, respectively. We calculated the log jam-induced hyporheic flow rate, $Q_{H,PIV}$, by subtracting the surface flow rate on the downstream side of the jam from the upstream surface flow rate, which was $Q_{H,PIV} = Q_{\text{up}} - Q_{\text{down}}$. For the cases without a porous log jam (Table 1, Cases F1 to F4), $Q_{H,PIV}$ was about -3% of Q_{up} (the cross symbols in Figure 4), showing that the hyporheic flow was small without a log jam. The small negative hyporheic flow rates (<5%) for the cases without a log jam were consistent with a slight increase in the mean streamwise surface flow velocity as the flow moved from the impermeable bed to the permeable sediment bed, according to conservation of mass (see Section 5.2 for details). The small negative hyporheic flow rate and the slight increase in streamwise mean flow velocity may be caused by the uncertainty associated with our velocity measurements and possible secondary flows that are common in flume experiments (Voermans et al., 2017). For cases with a log jam, the measured $Q_{H,PIV}$ was around 6% of Q_{up} when the Froude number Fr was less than 0.06. When Fr was above 0.06, the hyporheic flow rate increased sharply with increasing Fr and reached about 30% of Q_{up}. The sharp increase in $Q_{H,PIV}/Q_{\text{up}}$ at Fr above 0.06 suggests that hyporheic flow became increasingly significant at Fr above 0.06.

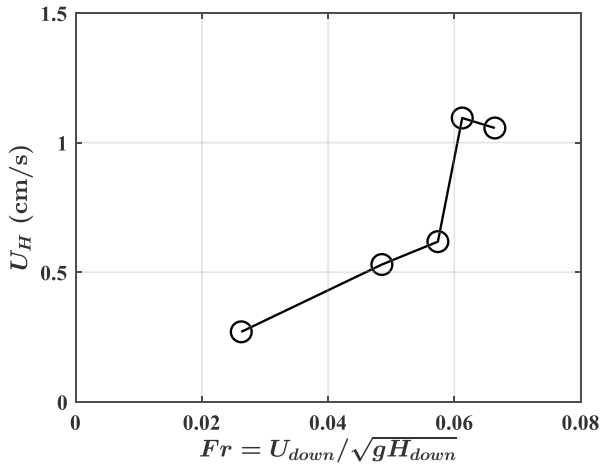

Figure 6. The depth-averaged hyporheic flow velocity within the sediment underneath the log jam, U_H, versus the Froude number on the downstream side of the log jam Fr. U_H was estimated from the dye visualization experiments, and the dye was injected at $y = 25$ cm.

4.3. The Hyporheic Flow Field in the Sediment Under a Log Jam

Dye visualization experiments were conducted to visualize the hyporheic flow path and calculate the hyporheic flow velocity within the sediment bed. A representative image for Case L1 (Table 1) is shown in Figure 5. From the hyporheic flow velocity field, we calculated the depth-averaged hyporheic flow velocity, U_H, at the downstream edge of the log jam (right dashed line in Figure 5b). The depth-averaged hyporheic flow velocity U_H in the sediment underneath the log jam is plotted against the Froude number on the downstream side of the log jam in Figure 6. As shown in Figure 6, when Fr was below 0.06, the hyporheic flow velocity increased slowly with increasing Fr. As Fr increased above 0.06, a sharp increase in U_H was observed. The sharp increase in U_H with Fr at $Fr > 0.06$ was consistent with the PIV measurements shown in Figure 4. The increase in U_H with Fr was also consistent with Equation 7, which suggests that hyporheic flow increases with increasing Fr. We also calculated the hyporheic flow rate $Q_{H,Dye}$ from U_H, that is, $Q_{H,Dye} = BH_sU_H$. The results are listed in Table 1. $Q_{H,Dye}$ estimated from the dye visualization was on the same order of magnitude as $Q_{H,PIV}$, the hyporheic flow rate measured by the PIV. We anticipated that $Q_{H,PIV}$ was a more accurate representation of the hyporheic flow rate because $Q_{H,Dye}$ was calculated based on the hyporheic flow field at $y = 25$ cm and did not capture the heterogeneity of the hyporheic flow field in the spanwise direction.

5. Discussions

5.1. Log Jam-Induced Turbulence and Water Surface Elevation Drop

As shown in Figures 4 and 6, both the hyporheic flow rate $Q_{H,PIV}$ and the hyporheic flow velocity U_H increased significantly when the Froude number Fr was larger than 0.06. The increase in hyporheic flow rate with increasing Fr was consistent with our model (Equation 7) and the previous model (Sawyer et al., 2011). Similar to the dependency of hyporheic flow rate on Fr, our results show that $Q_{H,PIV}$ and U_H remain less than 10% of Q_{up} and 1 cm/s, respectively, when the Reynolds number based on the frontal area of the log jam, $Re_v = U_{\log} r_v/\nu$, was smaller than 1,500 and increased sharply with increasing Re_v when $Re_v > 1{,}500$, as shown in Figures 7a and 7b. In addition, we also plotted $Q_{H,PIV}/Q_{\text{up}}$ and U_H versus the Reynolds number based on the hydraulic radius Re_h in Figures S16a and S16b in Supporting Information S1. Note that the dependency of Q_H on Re_v was nosier than the dependency of Q_H on Fr, suggesting that Fr was a primary parameter that controlled hyporheic flow as suggested by our model (Equation 7) and by Sawyer et al. (2011), and Reynolds number was a secondary parameter.

In addition, above the transitional Froude number and Reynolds number, sharp changes in turbulent intensity and water surface profile were observed. First, we measured the cross-sectionally averaged turbulent kinetic energy k_t on the downstream side of the log jam using a 2D PIV (see Section 3 for details). As shown in Figures 7c and 7d, k_t increases significantly when $Fr > 0.06$ and $Re_v > 1{,}500$. Second, we investigated the surface elevation for the cases with Froude number lower and higher than the transitional $Fr = 0.06$. As shown in Figure 8c and Figure S17 in Supporting Information S1, for flows with $Fr > 0.06$ and $Q_{H,PIV}/Q_{\text{down}}$ larger than 10%, the water surface elevation dropped (by up to 9% of H_{down}) a few centimeters downstream of the log jam and then raised to a steady value with increasing distance from the log jam. Such a drop in water surface elevation was not observed when $Fr < 0.06$ (Figures 8a and 8b) and $Q_{H,PIV}/Q_{\text{down}}$ was around 6%. While the mechanism of the transition behavior of the log jam-induced hyporheic flow has not been fully understood, our observations suggest that the drop in water surface elevation on the downstream side of the log jam can potentially be used to identify the transition when hyporheic flow becomes increasingly significant in the field.

5.2. The Negligible Impacts of the Bed Transition and the Log Jam-Induced Bedforms on Hyporheic Flows

Here we evaluate the impact of the transition of bed from impermeable bed to permeable bed at the upstream edge of the 1.5-m-long porous bed filled with sediment on the hyporheic flow. As shown in Figures 1 and 3a, the bed before the test section filled with hydrogel beads was impermeable. The transition from impermeable

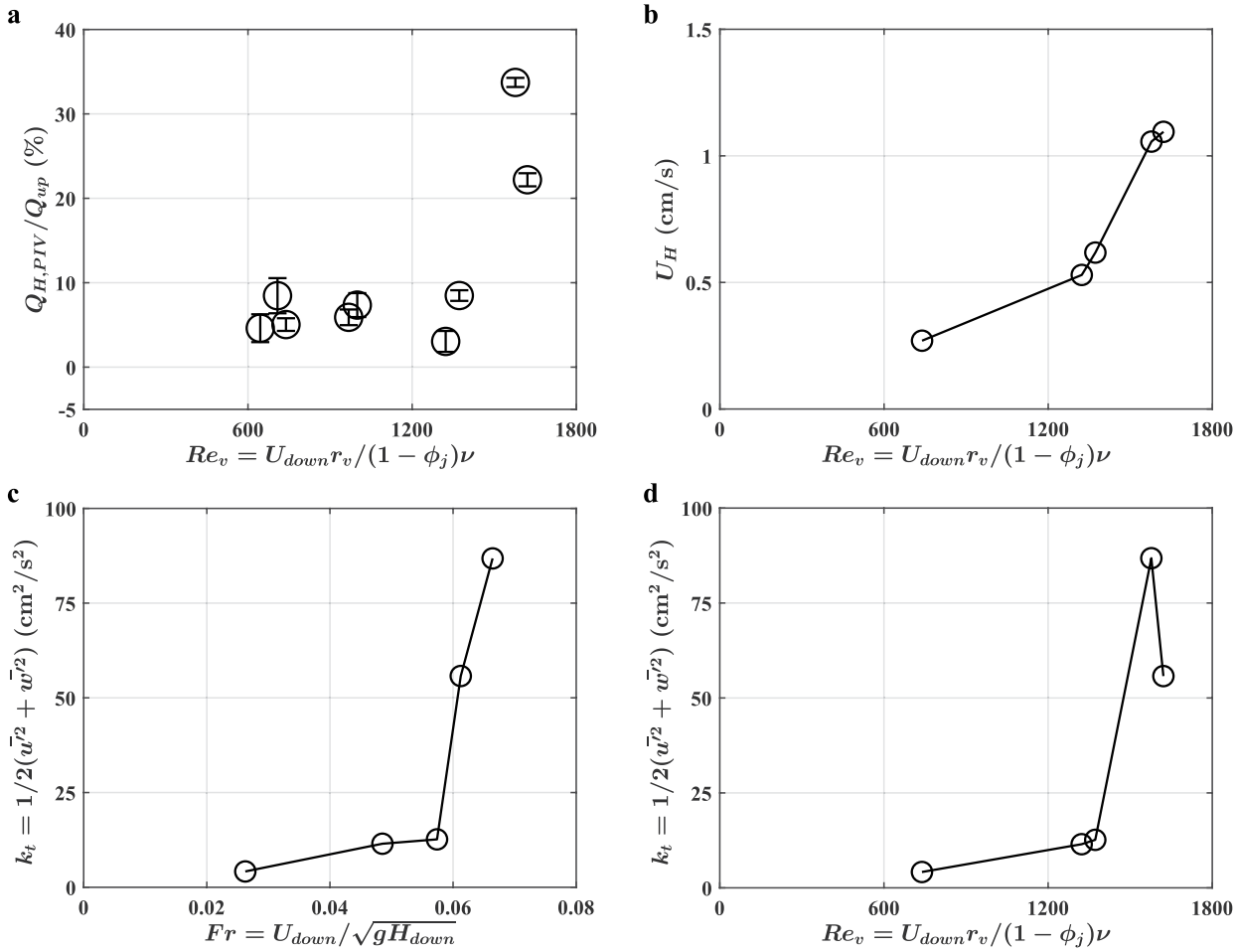

Figure 7. (a) The hyporheic flow rate $Q_{H,PIV}$ versus the Reynolds number Re_v. (b) The hyporheic velocity U_H versus the Reynolds number Re_v. (c) The measured turbulent kinetic energy of the surface flow on the downstream side of the log jam $k_{t,v+w} = \frac{1}{2}\left(\overline{u'^2} + \overline{w'^2}\right)$ versus the Froude number on the downstream side of the log jam Fr. (d) $k_{t,v+w}$ versus the Reynolds number Re_v.

to permeable beds may affect surface flow and, as such, affect the hyporheic flow. To evaluate such effects, we measured the surface flow velocity along a streamwise transect in the middle of the channel using a PIV for Case F1. The center of the log jam was located at $x = 0$ cm, and the edges of the log jam were located at $x = -4.5$ and 4.5 cm. As shown in Figure S15a of the Supporting Information S1, the depth-averaged surface flow velocity at the center of the channel increased by less than 5% along the streamwise transect (Figure S15b in Supporting Information S1), which was consistent with the small (<5%) negative hyporheic flow rates for the cases without a log jam. The increase in mean surface flow velocity along the streamwise direction and the negative hyporheic flow rates may be caused by the uncertainty in the surface flow measurements and/or the secondary flow pattern created by the surface flow separation at the impermeable-permeable transition (Voermans et al., 2017).

During the experiments with a log jam, bedforms were observed and became increasingly noticeable with increasing flow velocity. To evaluate the hyporheic flows induced by the bedform as well as by a flat bed, we calculated the hyporheic flow based on PIV measurements and dye visualization experiments in a channel with a flat bed and a channel with a log jam-induced bedform but without the log jam. For both cases, the mean flow velocity was $U_{up} = 8.2 \pm 0.1$ cm/s, the same as in Case L1 (Table 1). The PIV measurements showed that the differences between Q_{up} and Q_{down} are about 3% of Q_{up} for the cases without the log jam, regardless of the bedforms, suggesting that the impact of log jam-induced bedforms on the hyporheic flow was negligible compared with the impact of log jam.

In addition, for the cases with a flat bed, the mean hyporheic flow velocity U_H in streamwise direction was on the order of 10^{-4} cm/s (Figure 9b). For the case with a log jam-induced bedform but without the log jam,

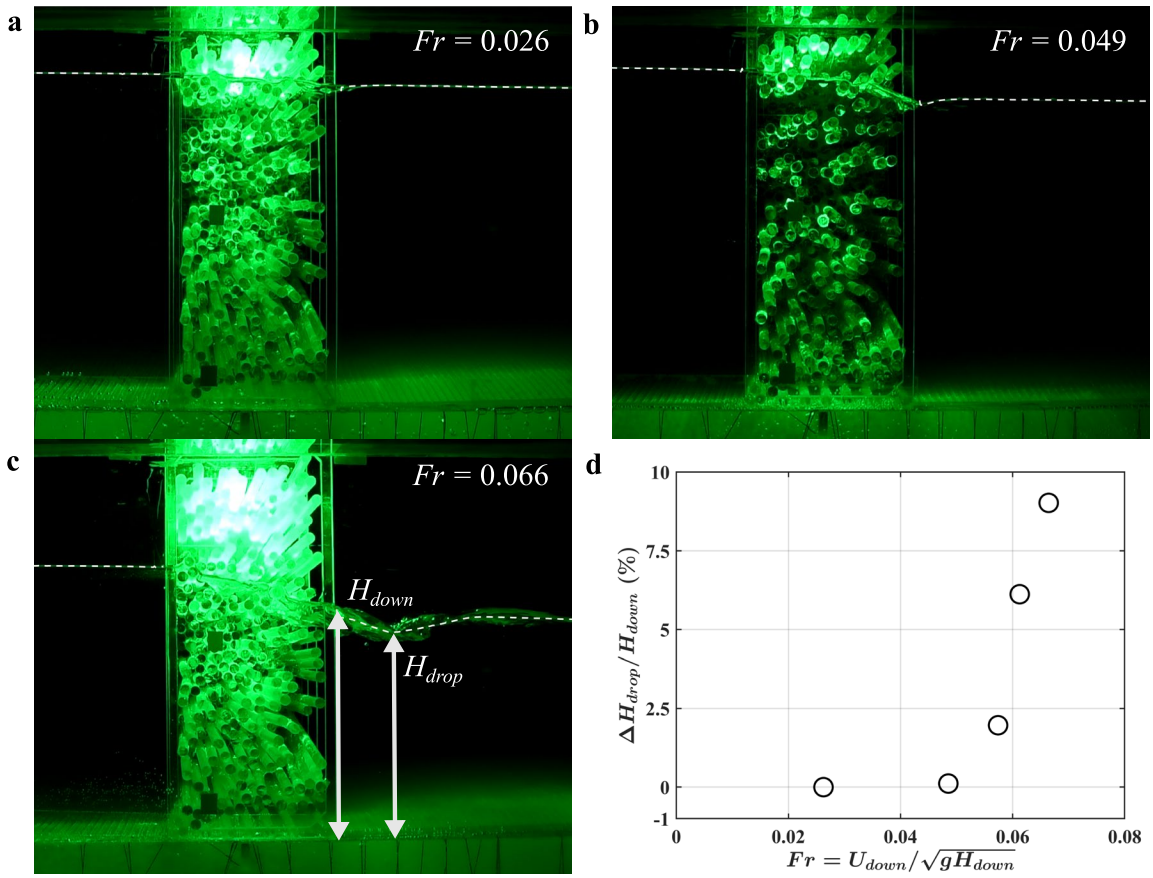

Figure 8. (a–c) Water surface profiles with various Froude numbers. (d) The largest water surface drop, $\Delta H_{\text{drop}} = H_{\text{down}} - H_{\text{drop}}$, versus the Froude number.

$U_H = 1.7 \times 10^{-3}$ cm/s (Figure 9c). The hyporheic flow velocity for both cases without a log jam was over two orders of magnitude smaller than $U_H = 0.5$ cm/s for the case with a log jam under the similar mean upstream surface flow velocity $U_H = 8.2 \pm 0.1$ cm/s (Figure 9a). The small hyporheic flow velocity for the case with log jam-induced bedforms but without a log jam, compared with the case with a log jam, further confirms that the hyporheic flow for the channels with log jams we observed was mainly contributed by the presence of log jam instead of the log jam-induced bed forms. Consistently, Sawyer et al. (2011) also showed that the impact of bedforms on hyporheic flow was smaller than a single channel-spanning log.

5.3. The Drag Coefficient and the Effective Permeability of the Log Jam

We calculated the drag coefficient of the log jam C_D from our experimental measurements based on Equation 4a. Specifically, we substituted the measured water depths and the surface flow velocity into Equation 4a, from which we calculated $C_D = \frac{H_{\text{up}}^2 - H_{\text{down}}^2}{H_{\text{down}} U_{\text{down}}^2} \frac{g(1-\phi_j)^3}{L_j a} = 2.6 \pm 0.2$ (standard deviation) (Figure 10a).

In addition, we calculated the effective permeability of the log jam k_j, a parameter that has been used in many numerical simulations (Doughty et al., 2020; Marshall et al., 2023; Xu & Liu, 2017). For the range of conditions used in our study (e.g., $\phi_j = 0.42$, $Fr = 0.026$ to 0.066), our calculations based on Equation 8 suggest $k_j = (6.7 \pm 2.3) \times 10^{-8}$ m^2, as shown in Figure 10b. If we assumed that the velocity head was negligible, namely $\Delta P = \frac{1}{2}\rho g\left(H_{\text{down}} - H_{\text{up}}\right)$, the resulting k_j was similar to k_j calculated with velocity head (Figure S21a in Supporting Information S1), because the magnitude of the velocity head difference was only 0.2% of the hydrostatic head difference. The effective permeability of the log jam k_j calculated using the Dupuit-Forchheimer equation was $k_j = (3.2 \pm 1.2) \times 10^{-8}$ m^2 (Figure S21b in Supporting Information S1), which was smaller than the k_j calculated based on Darcy's law ($k_j = (6.7 \pm 2.3) \times 10^{-8}$ m^2).

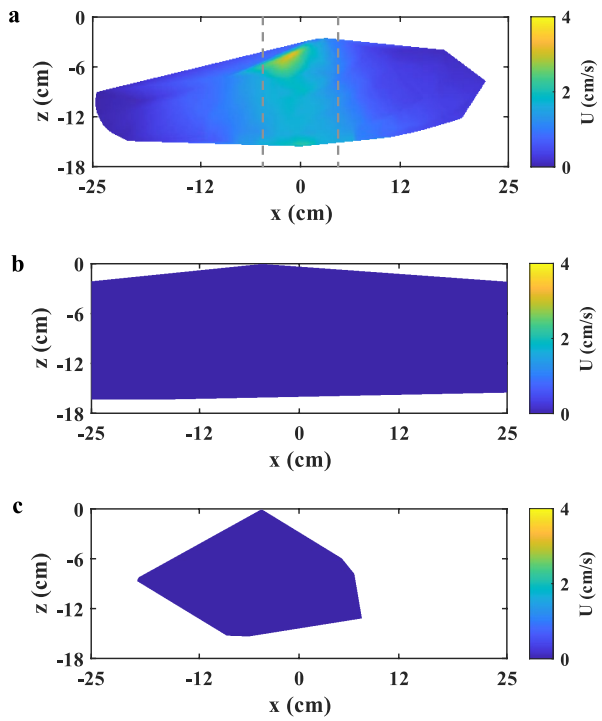

Figure 9. Color maps showing the hyporheic flow velocity in the streamwise direction for channels (a) with a log jam and log jam-induced bedform, (b) over a flat bed without a log jam, and (c) over a log jam-induced bedform but without a log jam. The mean surface velocity of surface water in the channel is $U_{up} = 8.2 \pm 0.1$ cm/s for all cases. Gray dashed vertical lines in (a) indicate the streamwise boundaries of the log jam. The dye was injected at $y = 25$ cm. The white areas are regions without hyporheic flow velocity measurements due to low hyporheic flow velocity, interference of the sediment-water interface, and scour holes. More details of the hyporheic velocity distribution for (b) and (c) can be found in Figure S18 of the Supporting Information S1.

Further, we observed a slight decrease in k_j with increasing Fr (Figure 10b; Figure S21 in Supporting Information S1). The values of k_j we measured and the k_j versus Fr relationship will facilitate future selection of parameters in numerical studies.

5.4. Justification of the Assumptions in the Theoretical Derivation

This section aims to justify the assumptions used in the theoretical derivation of Equation 7 based on our experimental measurements. First, we assumed that the drag force exerted by flow on our porous jam formed by piles of horizontal logs follows a quadratic law, similar to the drag on arrays of vertical dowels. In Section 5.3, we calculated the drag coefficient C_D by the measured water depths, surface flow velocities, and the log jam properties (Figure 10a). We compared our calculated C_D with the empirical model of C_D proposed by Cheng and Nguyen (2011) in Figure S19 in Supporting Information S1. Our calculated $C_D = 2.6 \pm 0.2$ fell in the range predicted by the previous model $C_D = 2.6 \pm 0.4$, suggesting that the C_D for a porous log jam can be approximated by the C_D in an array of the circular cylinders.

Second, we approximated the spatially averaged streamwise surface flow velocity within the log jam, U_{log}, as the surface flow velocity at the downstream edge of the log jam, namely $U_{log} = U_{down}/(1-\phi_j)$. For Case L1, $U_{down}/(1-\phi_j) = 13.7$ cm/s. We measured the mean surface flow velocity 2 cm upstream of the log jam for Case L1, in which $U_{up,2cm} = 7.3$ cm/s. The surface flow velocity at the upstream edge of the log jam was $U_{up,2cm}/(1-\phi_j) = 12.7$ cm/s. If we approximated U_{log} as the mean surface flow velocities at the upstream and downstream edges of the log jam, then $U_{log} = (12.7 + 13.7)/2 = 13.2$ cm/s. The difference between U_{log} and $U_{down}/(1-\phi_j)$ was only 3.6% of U_{log}, confirming that U_{log} can be approximated by $U_{down}/(1-\phi_j)$.

For the surface flow, we estimated the net momentum change of Equation 1 for Case L1, which was equal to $\rho B(1-\phi_j)\left(H_{down}U_{down}^2 - H_{up}U_{up}^2\right) = -8.8 \times 10^{-2}$ kg · m/s^2. The calculated net momentum change was less than 1% of the hydrostatic pressure force $\frac{1}{2}\rho g B(1-\phi_j)\left(H_{up}^2 - H_{down}^2\right) = 23.0$ kg · m/s^2, confirming that the net momentum change term in Equation 1 can be neglected. The assumption and our measurements of surface flow and water

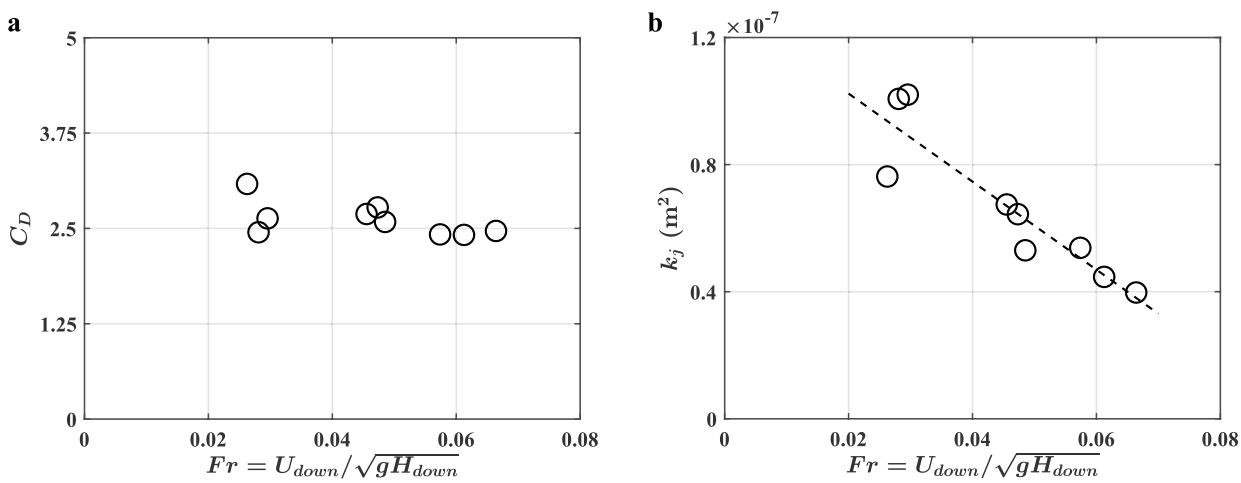

Figure 10. (a) The measured drag coefficients of the logs versus the Froude number. (b) The effective permeability of the log jam versus the Froude number. The black dash line ($y = (-13.9x + 1.3) \times 10^{-7}$) represents a linear regression line of k_j on Fr with $R^2 = 0.8$.

surface elevation were consistent with the surface flow experiments conducted by Follett et al. (2020) (Figure S20 in Supporting Information S1).

Finally, we assumed that the hydraulic pressure difference caused by the variation of the surface flow velocity on the upstream and downstream sides of the log jam, that is, $\frac{1}{2}\rho\left(U_{\text{down}}^2 - U_{\text{up}}^2\right)$, was much smaller than the difference in hydrostatic pressure, $\rho g(H_{\text{down}} - H_{\text{up}})$, and could be neglected. In all cases, $\frac{1}{2}\rho\left(U_{\text{down}}^2 - U_{\text{up}}^2\right)$ was less than 0.1% of the total hydraulic pressure difference, consistent with our hypothesis.

In this study, we quantified the hyporheic flow induced by a channel-spanning porous log jam with a solid volume fraction $\phi_j = 0.42$ and the downstream Froude number $Fr = 0.026$ to 0.066 on a flat gravel bed. To apply the results to natural log jams, the differences in the solid volume fractions, the range of the Froude number, and the different types and sizes of sediment need to be considered.

6. Conclusions

Here, we quantified the impact of a channel-spanning porous log jam, formed by piles of cylindrical logs, on hyporheic flow through laboratory flume experiments. Our results show that at the same mean surface flow velocity, the presence of a channel-spanning porous log jam increased the hyporheic flow velocity by two orders of magnitude. In addition, we showed that the log jam-induced hyporheic flow rate was about 6% of the total surface flow rate when the Froude number was less than 0.06. In contrast, this log jam-induced hyporheic flow rate increased with the Froude number to about 30% of the total surface flow rate when the Froude number was above 0.06. Consistently, our theoretical model suggested that the log jam-induced hyporheic flow rate scales with the square of the Froude number on the downstream side of the log jam. Similar to the dependency with Fr, the log jam-induced hyporheic flow also showed little variation when the Reynolds number was less than 1,500 and increased sharply when the Reynolds number was larger than 1,500. The sharp increase in hyporheic flow was accompanied by a sharp increase in turbulent kinetic energy and a noticeable water surface elevation dip on the downstream side of the log jam. Further, we quantified the effective permeability of the log jam. Our results have implications for future modeling of porous log jam-induced hyporheic flow and field estimation of such exchange based on surface flow measurements.

Data Availability Statement

The flow measurement and dye visualization data, along with the associated processing codes, have been deposited in the Data Repository for the University of Minnesota (Huang and Yang (2023), https://doi.org/10.13020/57f0-r060).

Acknowledgments
The research was supported by the National Science Foundation (EAR 2209591). The authors would like to thank Benjamin Erickson and Matthew Lueker for help with the modification of the flume and Jorge E. San Juan for help with the PIV system.

References

Ader, E., Wohl, E., McFadden, S., & Singha, K. (2021). Logjams as a driver of transient storage in a mountain stream. *Earth Surface Processes and Landforms*, *46*(3), 701–711. https://doi.org/10.1002/esp.5057

Boano, F., Camporeale, C., Revelli, R., & Ridolfi, L. (2006). Sinuosity-driven hyporheic exchange in meandering rivers. *Geophysical Research Letters*, *33*(18), L18406. https://doi.org/10.1029/2006gl027630

Boano, F., Demaria, A., Revelli, R., & Ridolfi, L. (2010). Biogeochemical zonation due to intrameander hyporheic flow. *Water Resources Research*, *46*(2), W02511. https://doi.org/10.1029/2008wr007583

Boano, F., Harvey, J. W., Marion, A., Packman, A. I., Revelli, R., Ridolfi, L., & Wörman, A. (2014). Hyporheic flow and transport processes: Mechanisms, models, and biogeochemical implications. *Reviews of Geophysics*, *52*(4), 603–679. https://doi.org/10.1002/2012rg000417

Boulton, A. J., Findlay, S., Marmonier, P., Stanley, E. H., & Valett, H. M. (1998). The functional significance of the hyporheic zone in streams and rivers. *Annual Review of Ecology and Systematics*, *29*(1), 59–81. https://doi.org/10.1146/annurev.ecolsys.29.1.59

Buffington, J. M., & Tonina, D. (2009). Hyporheic exchange in mountain rivers II: Effects of channel morphology on mechanics, scales, and rates of exchange. *Geography Compass*, *3*(3), 1038–1062. https://doi.org/10.1111/j.1749-8198.2009.00225.x

Cardenas, M. B. (2009). A model for lateral hyporheic flow based on valley slope and channel sinuosity. *Water Resources Research*, *45*(1), W01501. https://doi.org/10.1029/2008wr007442

Cheng, N. S., & Nguyen, H. T. (2011). Hydraulic radius for evaluating resistance induced by simulated emergent vegetation in open-channel flows. *Journal of Hydraulic Engineering*, *137*(9), 995–1004. https://doi.org/10.1061/(asce)hy.1943-7900.0000377

Curran, J. H., & Wohl, E. E. (2003). Large woody debris and flow resistance in step-pool channels, Cascade Range, Washington. *Geomorphology*, *51*(1–3), 141–157. https://doi.org/10.1016/s0169-555x(02)00333-1

Das, B. M. (2021). Principles of geotechnical engineering. *Cengage Learning*.

Dixon, S. J. (2016). A dimensionless statistical analysis of logjam form and process. *Ecohydrology*, *9*(6), 1117–1129. https://doi.org/10.1002/eco.1710

Doughty, M., Sawyer, A., Wohl, E., & Singha, K. (2020). Mapping increases in hyporheic exchange from channel-spanning logjams. *Journal of Hydrology*, *587*, 124931. https://doi.org/10.1016/j.jhydrol.2020.124931

Drummond, J. D., Nel, H. A., Packman, A. I., & Krause, S. (2020). Significance of hyporheic exchange for predicting microplastic fate in rivers. *Environmental Science and Technology Letters*, *7*(10), 727–732. https://doi.org/10.1021/acs.estlett.0c00595

Dudunake, T., Tonina, D., Reeder, W., & Monsalve, A. (2020). Local and reach-scale hyporheic flow response from Boulder-induced geomorphic changes. *Water Resources Research*, *56*(10), e2020WR027719. https://doi.org/10.1029/2020wr027719

Elliott, A. H., & Brooks, N. H. (1997). Transfer of nonsorbing solutes to a streambed with bed forms: Theory. *Water Resources Research*, *33*(1), 123–136. https://doi.org/10.1029/96wr02784

Endreny, T., Lautz, L., & Siegel, D. (2011). Hyporheic flow path response to hydraulic jumps at river steps: Flume and hydrodynamic models. *Water Resources Research*, *47*(2), W02517. https://doi.org/10.1029/2009wr008631

Follett, E., Schalko, I., & Nepf, H. (2020). Momentum and energy predict the backwater rise generated by a large wood jam. *Geophysical Research Letters*, *47*(17), e2020GL089346. https://doi.org/10.1029/2020gl089346

Follett, E., Schalko, I., & Nepf, H. (2021). Logjams with a lower gap: Backwater rise and flow distribution beneath and through logjam predicted by two-box momentum balance. *Geophysical Research Letters*, *48*(16), e2021GL094279. https://doi.org/10.1029/2021gl094279

Gooseff, M. N. (2010). Defining hyporheic zones–advancing our conceptual and operational definitions of where stream water and groundwater meet. *Geography Compass*, *4*(8), 945–955. https://doi.org/10.1111/j.1749-8198.2010.00364.x

Huang, S. H., & Yang, J. Q. (2022). Impacts of emergent vegetation on hyporheic exchange. *Geophysical Research Letters*, *49*(13), e2022GL099095. https://doi.org/10.1029/2022gl099095

Huang, S. H., & Yang, J. Q. (2023). Experimental data of log jam-induced hyporheic flow experiment in Ecoflume of St. Anthony Falls Laboratory on 2022 (116GB) [Dataset]. DRUM. https://doi.org/10.13020/57f0-r060

Ismail, H., Xu, Y., & Liu, X. (2021). Flow and scour around idealized porous engineered log jam structures. *Journal of Hydraulic Engineering*, *147*(1), 04020089. https://doi.org/10.1061/(asce)hy.1943-7900.0001833

Jaeger, A., Posselt, M., Schaper, J. L., Betterle, A., Rutere, C., Coll, C., et al. (2021). Transformation of organic micropollutants along hyporheic flow in bedforms of river-simulating flumes. *Scientific Reports*, *11*(1), 1–18. https://doi.org/10.1038/s41598-021-91519-2

Janzen, K., & Westbrook, C. J. (2011). Hyporheic flows along a channelled peatland: Influence of beaver dams. *Canadian Water Resources Journal/Revue Canadienne des Ressources Hydriques*, *36*(4), 331–347. https://doi.org/10.4296/cwrj3604846

Jin, G., Zhang, S., Zhou, B., Yang, Y., Zhang, Z., Chen, H., & Tang, H. (2023). Solute transport characteristics in the streambed due to rigid non-submerged plants: Experiment and simulations. *Journal of Hydrology*, *619*, 129315. https://doi.org/10.1016/j.jhydrol.2023.129315

Lautz, L. K., Siegel, D. I., & Bauer, R. L. (2006). Impact of debris dams on hyporheic interaction along a semi-arid stream. *Hydrological Processes*, *20*(1), 183–196. https://doi.org/10.1002/hyp.5910

Lehane, B., Giller, P., O'halloran, J., Smith, C., & Murphy, J. (2002). Experimental provision of large woody debris in streams as a trout management technique. *Aquatic Conservation: Marine and Freshwater Ecosystems*, *12*(3), 289–311. https://doi.org/10.1002/aqc.516

Li, A., Aubeneau, A. F., Bolster, D., Tank, J. L., & Packman, A. I. (2017). Covariation in patterns of turbulence-driven hyporheic flow and denitrification enhances reach-scale nitrogen removal. *Water Resources Research*, *53*(8), 6927–6944. https://doi.org/10.1002/2016wr019949

Livers, B., Lininger, K. B., Kramer, N., & Sendrowski, A. (2020). Porosity problems: Comparing and reviewing methods for estimating porosity and volume of wood jams in the field. *Earth Surface Processes and Landforms*, *45*(13), 3336–3353. https://doi.org/10.1002/esp.4969

Majerova, M., Neilson, B., Schmadel, N., Wheaton, J., & Snow, C. (2015). Impacts of beaver dams on hydrologic and temperature regimes in a mountain stream. *Hydrology and Earth System Sciences*, *19*(8), 3541–3556. https://doi.org/10.5194/hess-19-3541-2015

Marion, A., Bellinello, M., Guymer, I., & Packman, A. (2002). Effect of bed form geometry on the penetration of nonreactive solutes into a streambed. *Water Resources Research*, *38*(10), 27-21–27-12. https://doi.org/10.1029/2001wr000264

Marshall, A., Zhang, X., Sawyer, A. H., Wohl, E., & Singha, K. (2023). Logjam characteristics as drivers of transient storage in headwater streams. *Water Resources Research*, *59*(3), e2022WR033139. https://doi.org/10.1029/2022wr033139

McCallum, J. L., Höhne, A., Schaper, J. L., Shanafield, M., Banks, E. W., Posselt, M., et al. (2020). A numerical stream transport modeling approach including multiple conceptualizations of hyporheic exchange and spatial variability to assess contaminant removal. *Water Resources Research*, *56*(3), e2019WR024987. https://doi.org/10.1029/2019wr024987

Naganna, S. R., Deka, P. C., Ch, S., & Hansen, W. F. (2017). Factors influencing streambed hydraulic conductivity and their implications on stream–aquifer interaction: A conceptual review. *Environmental Science and Pollution Research*, *24*(32), 24765–24789. https://doi.org/10.1007/s11356-017-0393-4

Nepf, H. M. (2012). Flow and transport in regions with aquatic vegetation. *Annual Review of Fluid Mechanics*, *44*(1), 123–142. https://doi.org/10.1146/annurev-fluid-120710-101048

Packman, A. I., Brooks, N. H., & Morgan, J. J. (2000). Kaolinite exchange between a stream and streambed: Laboratory experiments and validation of a colloid transport model. *Water Resources Research*, *36*(8), 2363–2372. https://doi.org/10.1029/2000wr900058

Packman, A. I., Salehin, M., & Zaramella, M. (2004). Hyporheic exchange with gravel beds: Basic hydrodynamic interactions and bedform-induced advective flows. *Journal of Hydraulic Engineering*, *130*(7), 647–656. https://doi.org/10.1061/(asce)0733-9429(2004)130:7(647)

Roche, K., Blois, G., Best, J., Christensen, K., Aubeneau, A., & Packman, A. (2018). Turbulence links momentum and solute exchange in coarse-grained streambeds. *Water Resources Research*, *54*(5), 3225–3242. https://doi.org/10.1029/2017wr021992

Roche, K. R., Li, A., Bolster, D., Wagner, G. J., & Packman, A. I. (2019). Effects of turbulent hyporheic mixing on reach-scale transport. *Water Resources Research*, *55*(5), 3780–3795. https://doi.org/10.1029/2018wr023421

Rousseau, G., & Ancey, C. (2020). Scanning PIV of turbulent flows over and through rough porous beds using refractive index matching. *Experiments in Fluids*, *61*(8), 1–24. https://doi.org/10.1007/s00348-020-02990-y

Sawyer, A. H., Bayani Cardenas, M., & Buttles, J. (2011). Hyporheic exchange due to channel-spanning logs. *Water Resources Research*, *47*(8), W08502. https://doi.org/10.1029/2011wr010484

Schalko, I., Schmocker, L., Weitbrecht, V., & Boes, R. M. (2018). Backwater rise due to large wood accumulations. *Journal of Hydraulic Engineering*, *144*(9), 04018056. https://doi.org/10.1061/(asce)hy.1943-7900.0001501

Schaper, J. L., Posselt, M., Bouchez, C., Jaeger, A., Nuetzmann, G., Putschew, A., et al. (2019). Fate of trace organic compounds in the hyporheic zone: Influence of retardation, the benthic biolayer, and organic carbon. *Environmental Science & Technology*, *53*(8), 4224–4234. https://doi.org/10.1021/acs.est.8b06231

Scott, D. N., Montgomery, D. R., & Wohl, E. E. (2014). Log step and clast interactions in mountain streams in the central Cascade Range of Washington State, USA. *Geomorphology*, *216*, 180–186. https://doi.org/10.1016/j.geomorph.2014.04.004

Spreitzer, G., Tunnicliffe, J., & Friedrich, H. (2020). Porosity and volume assessments of large wood (LW) accumulations. *Geomorphology*, *358*, 107122. https://doi.org/10.1016/j.geomorph.2020.107122

Spreitzer, G., Tunnicliffe, J., & Friedrich, H. (2021). Effects of large wood (LW) blockage on bedload connectivity in the presence of a hydraulic structure. *Ecological Engineering*, *161*, 106156. https://doi.org/10.1016/j.ecoleng.2021.106156

Stonedahl, S. H., Harvey, J. W., Detty, J., Aubeneau, A., & Packman, A. I. (2012). Physical controls and predictability of stream hyporheic flow evaluated with a multiscale model. *Water Resources Research*, *48*(10), W10513. https://doi.org/10.1029/2011wr011582

Thielicke, W., & Sonntag, R. (2021). Particle image velocimetry for MATLAB: Accuracy and enhanced algorithms in PIVlab. *Journal of Open Research Software*, *9*(1), 12. https://doi.org/10.5334/jors.334

Tonina, D. (2012). Surface water and streambed sediment interaction: The hyporheic exchange. *Fluid Mechanics of Environmental Interfaces*, 255–294.

Tonina, D., & Buffington, J. M. (2007). Hyporheic exchange in gravel bed rivers with pool-riffle morphology: Laboratory experiments and three-dimensional modeling. *Water Resources Research*, *43*(1), W01421. https://doi.org/10.1029/2005wr004328

Voermans, J. J., Ghisalberti, M., & Ivey, G. (2017). The variation of flow and turbulence across the sediment–water interface. *Journal of Fluid Mechanics*, *824*, 413–437. https://doi.org/10.1017/jfm.2017.345

Voermans, J. J., Ghisalberti, M., & Ivey, G. N. (2018a). A model for mass transport across the sediment-water interface. *Water Resources Research*, *54*(4), 2799–2812. https://doi.org/10.1002/2017wr022418

Voermans, J. J., Ghisalberti, M., & Ivey, G. N. (2018b). The hydrodynamic response of the sediment-water interface to coherent turbulent motions. *Geophysical Research Letters*, *45*(19), 10520–510527. https://doi.org/10.1029/2018gl079850

Wallerstein, N., & Thorne, C. (2004). Influence of large woody debris on morphological evolution of incised, sand-bed channels. *Geomorphology*, *57*(1–2), 53–73. https://doi.org/10.1016/s0169-555x(03)00083-7

Wilhelmsen, K., Sawyer, A., Marshall, A., McFadden, S., Singha, K., & Wohl, E. (2021). Laboratory flume and numerical modeling experiments show log jams and branching channels increase hyporheic exchange. *Water Resources Research*, *57*(9), e2021WR030299. https://doi.org/10.1029/2021wr030299

Wohl, E. (2016). Spatial heterogeneity as a component of river geomorphic complexity. *Progress in Physical Geography*, *40*(4), 598–615. https://doi.org/10.1177/0309133316658615

Wohl, E., & Scamardo, J. E. (2021). The resilience of logjams to floods. *Hydrological Processes*, *35*(1), e13970. https://doi.org/10.1002/hyp.13970

Xu, Y., & Liu, X. (2017). Effects of different in-stream structure representations in computational fluid dynamics models—Taking engineered log jams (ELJ) as an example. *Water*, *9*(2), 110. https://doi.org/10.3390/w9020110

Yuan, Y., Chen, X., Cardenas, M. B., Liu, X., & Chen, L. (2021). Hyporheic exchange driven by submerged rigid vegetation: A modeling study. *Water Resources Research*, *57*(6), e2019WR026675. https://doi.org/10.1029/2019wr026675